Advanced nanocomposite materials made of TiC nanocrystals in situ immobilized in SiC foams with boosted spectral selectivity

Maxime Balestrat, Maxime Cheype, Christel Gervais, Xavier Deschanels, Samuel Bernard

Materials Advances

ROYAL SOCIETY OF CHEMISTRY

PAPER

View Article Online
View Journal

Cite this: DOI: 10.1039/d2ma00886f

Advanced nanocomposite materials made of TiC nanocrystals *in situ* immobilized in SiC foams with boosted spectral selectivity†

Maxime Balestrat,*[a] Maxime Cheype,[a] Christel Gervais,[b] Xavier Deschanels[c] and Samuel Bernard*[a]

TiC/SiC nanocomposites have been prepared and fully characterized at various length scales before exploring their spectral selectivity for their exploitation as solar selective absorbers. The full design process consists of (i) performing the reaction between a polysilazane, namely Durazane® 1800, and tetrakis(dimethylamino)titanium, (ii) shaping the as-synthesized polymer into pellets, (iii) pyrolyzing in flowing argon the raw pellets in order to achieve the conversion of the polymer into a single-phase ceramic and (iv) performing a heat-treatment at higher temperature to generate nanocomposite structures while developing the porosity of the pellets. The evolutive material is characterized at each step of the process *via* a combination of complementary techniques including FTIR and solid-state NMR spectroscopies, elemental analyses, thermogravimetric analysis (TGA) coupled with mass spectroscopy (MS), X-ray diffraction (XRD), Raman spectroscopy, scanning electron microscopy (SEM), energy-dispersive X-ray spectroscopy (EDX) and transmission electron microscopy (TEM). The optical properties (0.25–25 μm wavelength range) of the materials have been explored as a function of the temperature at which the final material has been isolated (1000–1800 °C). The material prepared at 1800 °C made of TiC nanocrystals *in situ* immobilized in a highly crystallized SiC matrix with an open porosity of 56% exhibited a boosted room temperature spectral selectivity of 1.91 which has been so far the highest referenced among SiC-based materials.

Received 5th September 2022,
Accepted 11th January 2023

DOI: 10.1039/d2ma00886f

rsc.li/materials-advances

Introduction

Photothermal conversion of solar energy is a safe sustainable energy supply which has been attracting growing research interest to boost the burgeoning research field of Concentrating Solar Power (CSP) systems in recent years.[1] Photothermal conversion takes place in the first step in CSP using solar selective absorbers (SSAs). The SSAs – proposed by Tabor in the 1950s – are in thermal contact with a fluid or a gas to create steam which runs a turbine to produce electrical power in the second step.[2] Thus, SSAs are seen as the key materials which govern the overall performance of CSP.[3]

A first requirement to design SSAs relies on a high absorbance ($\alpha > 90\%$, low reflectance R) in the wavelength range of 0.3–2.5 μm (spectral region of the solar radiation) and a low thermal emittance ($\varepsilon < 10\%$, high reflectance R) in the infrared region (2.5–25 μm). This will contribute to an appropriate spectral selectivity (α/ε) which is the parameter to qualify the material composing SSAs.[4] A second requirement is its working temperature. Indeed, the current maximum operating temperature of SSAs is limited to 600 °C due to the degradation of its components above this temperature.[5] This significantly limits the full exploitation of the photothermal conversion of solar radiation for CSP. Higher working temperatures (typically 900 °C is a common target) will have the consequence of improving the efficiency of the thermal-to-electricity conversion of the power generation system which is capped by the Carnot efficiency; $\eta_c = 1 - T_c/T_h$ in which T_h is the working temperature and T_c is the ambient temperature,[6] thereby boosting the efficiency of SSAs.

Silicon carbide (SiC) offers unique features for high temperature applications compatible with the operating conditions of further CSP systems.[7] It is light weight, and has a high thermal conductivity, an excellent thermal shock resistance performance, a high strength and an oxidation resistance because of its capability to form a passivating oxide layer upon oxidation which provides a thermal stability up to ~1400 °C.[7–9] However, despite its good sunlight absorption properties, SiC displays a high thermal emittance in the infrared region leading to poor optical selectivity.[10]

[a] IRCER, CNRS, Univ. Limoges, Limoges, France.
E-mail: maxime.balestrat@unilim.fr, samuel.bernard@unilim.fr
[b] Sorbonne Université, CNRS, Collège de France, Laboratoire Chimie de la Matière Condensée de Paris, 4 Place de Jussieu, 75005 Paris, France
[c] Univ. Montpellier, ICSM, CEA, CNRS, ENSCM, Marcoule, France

† Electronic supplementary information (ESI) available. See DOI: https://doi.org/10.1039/d2ma00886f

Ultra-High Temperature Ceramics (UHTC, *e.g.* borides, carbides and some nitrides of early transition metals (TM)) can be considered as a class of promising materials in the field of solar thermal power. They possess favorable properties as solar absorbers such as a very high melting point, a good thermo-mechanical properties at high temperatures and, most of them are intrinsically selective.[10–17] Among those materials, TiC and TiN exhibit an inherent spectral selectivity which can be used for delivering high-performance SSAs.[17–19] However, they tend to oxidize in the targeted operating temperature range.[20–22] As most single-phase materials do not naturally have the required behavior (in terms of both thermal stability and spectral selectivity) as SSAs, how can we further enhance the working temperature of SSAs beyond 600 °C?

Engineered composites combining SiC with its unique features as a matrix surrounding the UHTC phase with its inherent spectral selectivity and a lower thermal emittance would display a combination of properties which can be advantageously exploited to increase the operating temperature of SSAs in the next generation of CSP systems. If such materials can be developed as porous components, they could be able to produce the so-called volumetric effect, which means that the irradiated side of the absorber is at a lower temperature than the medium leaving the absorber. Thus, the porous structure would act as a convective heat exchanger where the heat transfer fluid (*i.e.*, air) is imposed to maximize the absorption of the solar radiation by convection heat transfer mode. However, designing UHTC/SiC composites while developing the porosity is highly challenging.

The Polymer-Derived Ceramics (PDCs) route – *via in situ* growth and materials nano-structuring[23,24] represents an effective precursor approach for designing and synthesizing porous SiC – acting as a matrix – containing *in situ* generated nanoscale UHTC such as nanoTiC[25] or nanoTiN.[26]

Herein, the synthesis and processing of porous nanocomposites consisting of TiC nanocrystals which are *in situ* generated in a SiC matrix upon modification of preceramic polymers with Ti-containing precursors (tetrakis(dimethylamino)-titanium, $Ti[N(CH_3)_2]_4$) is addressed. As a preceramic polymer, we have selected a commercially available polysilazane, Durazane® 1800, which is well known to produce silico carbonitride (SiCN) ceramics[27,28] at intermediate temperatures and form SiC at higher temperatures because of the occurrence of carbothermal reduction reactions releasing nitrogen while developing the porosity of the material. The schematic representation of our approach is described in Fig. 1. The material has been characterized at each step of the process and we propose extensive chemical, structural and textural characterizations of the final nanocomposites. As a proof of concept, their spectral selectivity has been investigated at room temperature.

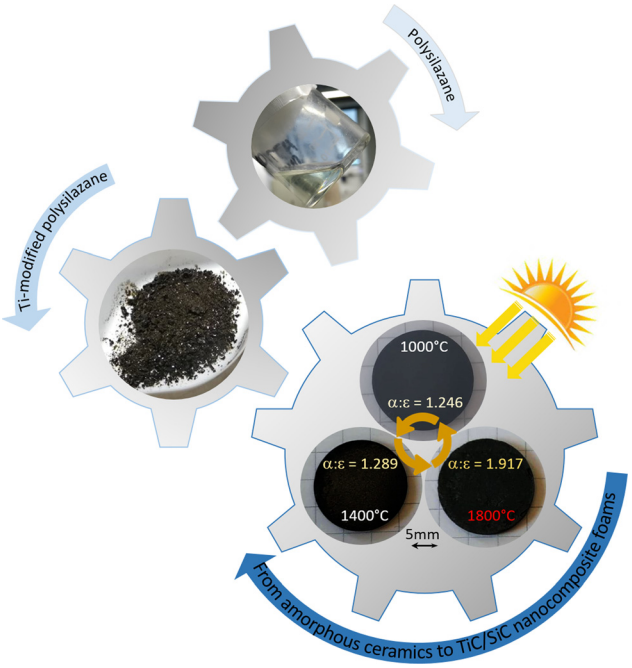

Fig. 1 Schematic diagram of the general process of designing SiC-based nanocomposite foams from Ti-modified polysilazanes and the provided chemical, structural and optical fingerprints.

Experimental

Materials

The synthesis of the precursor is carried out in a purified argon atmosphere passing through a column of phosphorus pentoxide and then through a vacuum/argon line by means of standard Schlenk techniques. The cleaned glassware is stored in an oven at 95 °C overnight before being connected to the vacuum/argon line, assembled and pumped under vacuum for 30 min and then filled with argon. All chemical products are handled in an argon-filled glove box (Jacomex, Campus-type; O_2 and H_2O concentrations kept at $\leq$0.1 ppm and $\leq$0.8 ppm, respectively). Toluene (99.85%, Extra Dry over Molecular Sieve, AcroSeal(R)) was purchased from Acros Organics™. The Durazane® 1800 labeled here PSZ was provided in a 5L container by Merck company, Germany, stored in a fridge and used as-received. Anal. found (wt%): Si, 41.3; C, 27.3; N, 22.7; H, 8.3; O, 0.4. $[Si1_{1.0}C_{1.5}N_{1.1}H_{5.5}]_n$ (normalized to total 100 wt% (total of wt% was 98.9 wt%) and referenced to $Si_{1.0}$. Oxygen content (below 2 wt%) was omitted in the empirical formulae). FTIR (ATR/cm^{-1}): ν(N–H) = 3381 (s), ν(C–H in vinyl) = 3058 (m), ν(C–H in methyl) = 2954 (s), 2902 (m) and 2848 (w), ν(Si–H) = 2123 (s), δ(C═C) = 1594 (w), δ(═C–H) = 1405 (w), δ(Si–CH_3) = 1251 (m), δ(N–H): 1169 (s), δ(C═C/═CH_2) = 947 (w), ν(N–Si–N) = 897 (vs), δ(Si–CH_3) = 787 (m); ^{1}H NMR (300 MHz, $CDCl_3$, δ/ppm): 0.4–0.1 (br, $SiCH_3$), 1.1–0.5 (br, NH), 4.9–4.4 (br, SiH), 6.3–5.7 (br, vinyl). Tetrakis(dimethylamino)titanium ($Ti[N(CH_3)_2]_4$, 99.99% trace metal basis) was obtained from Acros Organics™, stored in a fridge and used without further purification. It is labeled TDMAT.

Precursor synthesis

The reaction between PSZ and TDMAT occurs at toluene reflux in a three-neck round-bottom flask. In a typical experiment, 2.8 g of TDMAT (8.10 mmol) are quickly added with a syringe

under flowing argon to a solution of 2.7 g of PSZ (41.2 mmol referred to the theoretical monomeric unit of the polymer) in 80 mL of toluene at RT under vigorous stirring. Then, the temperature is increased up to toluene reflux under static argon and kept at this temperature under vigorous stirring for three days. After cooling down, the solvent is extracted *via* an ether bridge (100 °C/0.1 mbar) to release an air- and moisture-sensitive titanium-modified PSZ labeled **PSZTi5** (5 being the Si : Ti ratio) that appears as a brownish-black powder. Anal. Found (wt%): Si 30.1, Ti 10.2, C 29.4, N 21.2, H 7.5, O 1.6. $[Si_{1.0}Ti_{0.2}C_{2.3}N_{1.4}H_{6.9}]_n$ (normalized to total 100 wt % (total of wt% was 99.2 wt%) and referenced to $Si_{1.0}$ and oxygen content (below 2 wt%) was omitted in the empirical formulae). FTIR (ATR/cm^{-1}): ν(N–H) = 3384 (w), ν(C–H in vinyl) = 3046 (m), ν(C–H in methyl) 2960 (s) and 2893 (m), ν(C–H in methylamino groups): 2848 (s), 2789 (s), ν(Si–H) = 2121 (s), ν(C=C) = 1591 (w), $\delta(CH_3)$ = 1457 (m), $\delta(CH_2)$ = 1401 (s), ν(C–N) = 1294 (m), δ(Si–CH_3) = 1255 (s), δ(N–H): 1176 (s), $\nu_{as}(NC2)$ = 994 (m), $\nu_s(NC_2)$ = 951 (w), ν(N–Si–N) = 897 (vs), δ(Si–CH_3): 787 (m), ν(Ti–N) = 590 (w).

Precursor processing

The as-synthesized polymer is placed in alumina boats to be introduced in a sealed tube under an argon atmosphere to prevent any oxygen contamination of the sample during the transfer to the furnace. The polymeric powders is then introduced under an argon flow into a silica tube from a horizontal furnace (Carbolite BGHA12/450B). The tube is evacuated (0.1 mbar) for 30 min and refilled with argon (99.995%) to atmospheric pressure. Subsequently, the samples are subjected to a cycle of ramping of 5 °C min^{-1} to 1000 °C in flowing argon (dwelling time of 2 h at 1000 °C). A constant flow (120 mL min^{-1}) of argon is passed through the tube during the pyrolysis cycle. After cooling under an argon atmosphere, samples are stored in a glove-box for characterization. Samples are labeled **PSZTi5_10** with 10 being the two first digits of the temperature at which the polymer has been exposed. For higher temperature investigations (T > 1000 °C), the as-pyrolyzed samples are subsequently introduced in a graphite furnace (Nabertherm VHT-GR) to be pumped under vacuum (0.1 mbar), refilled with argon and maintained under a constant flow of argon (200 mL min^{-1}) during the whole heat treatment. The program consisted of a 5 °C min^{-1} heating ramp up to the maximum temperature fixed in the range 1400–1800 °C, dwelling at the selected temperature for 2 h and cooling down to RT at 5 °C min^{-1}. The samples are labeled **PSZTi5**-T with T being the two first digits of the temperature at which the polymer had been exposed (14 for 1400, 16 for 1600 and 18 for 1800 °C).

In order to design foams, **PSZTi5** is introduced in a sealed stainless-steel bowl in the glove-box to be then ball milled at 200 rpm for 40 min. Then, 1 g of each of the ball-milled **PSZTi5** powder is introduced in a heated steel die (AINT-25-H with a 25 mm internal diameter) in the glove-box then uniaxially pressed using a Specac Atlas Autotouch Press-40T at 80 MPa and heated to the set temperature (80 °C) at a heating rate of 5 °C min^{-1}. The selected temperature and pressure are held for 0.5 h. The pressure applied on the samples is then slowly deloaded during cooling down to RT within 1 h. Typical dimensions of the cylindrical green bodies are of a diameter of 25 mm and a thickness of 1.5 mm. The pyrolysis procedure differs from those applied for powders: the pelleted samples are subjected to a cycle of ramping of 1 °C min^{-1} to 1000 °C, dwelling there for 2 h, and then cooling down to RT at 2 °C min^{-1}. The high temperature treatment procedure matches that applied for powders.

Characterization

As the polymers are reactive towards moisture and oxygen, the following sample preparations were performed within a glove box. The chemical structure of polymers was determined by transmission FTIR spectroscopy using a Nicolet Magna 550 Fourier transform-infrared spectrometer. ^{1}H NMR data of PSZ solutions in $CDCl_3$ were obtained using a Bruker AM 300 spectrometer operating at 300 MHz. Tetramethylsilane (TMS) was used as a reference for the NMR data. Solid-state ^{13}C CP MAS and ^{29}Si MAS NMR spectra of solid samples were recorded on a Bruker AVANCE 300 spectrometer (7.0 T, $\nu_0(^1H)$ = 300.29 MHz, $\nu_0(^{13}C)$ = 75.51 MHz, $\nu_0(^{29}Si)$ = 59.66 MHz) using a 4 mm Bruker probe at a spinning frequency of 10 kHz. ^{13}C CP MAS experiments were recorded with ramped-amplitude cross-polarization in the ^{1}H channel to transfer magnetization from ^{1}H to ^{13}C. (Recycle delay = 3 s, CP contact time = 1 ms, optimized ^{1}H spinal-64 decoupling.) Single pulse ^{29}Si MAS NMR spectra were recorded with a recycle delay of 60 s. Chemical analyses of the polymers were performed by hot gas extraction techniques using a Horiba Emia-321V for carbon content and using a Horiba EMGA-830 for oxygen, nitrogen and hydrogen contents. The Si and Ti contents of the polymer have been measured at Mikroanalytisches Labor Pascher (Remagen, Germany). Thermogravimetric analyses (TGA) of samples were performed in flowing argon at 5 °C min^{-1} in a two-step process. The first step has been achieved up to 1000 °C using alumina crucibles at ambient atmospheric pressure (STA 449 F3, Netzsch GmbH, Selb, Germany) coupled with a mass spectrometer (Omnistar, Pfeiffer Vacuum GmbH, Asslar, Germany) at the outlet. The second step consisted to pyrolyze samples heat-treated at 1000 °C in a tungsten carbide crucible up to 1800 °C using a Setaram, Setsys apparatus. Elemental analyses of the pyrolyzed powders were carried out by EDS as well as by hot gas extraction techniques for carbon content using a Horiba Emia-321V and for oxygen, nitrogen and hydrogen contents using a Horiba EMGA-830. The Si and Ti contents of the pyrolyzed powders were determined by Inductively Coupled Plasma-Optical Emission Spectrometry (ICP-OES) using a PerkinElmer Optima 8300 instrument. The phase composition of ceramic samples was determined by XRD analyses (Bruker AXS D8 Discover, CuKα radiation, Billerica, Massachusetts, USA). The scans were performed in the range of $2\theta \in \langle 20°; 90°\rangle$ with a step of 0.015° and an exposure time of 0.7 s. The diffractograms were analyzed using the Diffrac + EVA software with the JCPDS-ICDD database. Raman spectroscopy micro-analyses were carried out with a Renishaw InViaReflex using 2

excitation laser wavelengths of 532 nm and 785 nm. The density of nanocomposite objects was investigated by hydrostatic weighing and compared to those of crushed powders studied by Helium pycnometry (Micromeritics, AccucPyc II 1340). Polished-bulk materials and also powders were observed using a JEOL IT300 scanning electron microscope. These microstructural observations were completed by chemical analyses using an Oxford X-ray dispersive spectrometer (EDX). Further observation on powders was done by transmission electron microscopy (TEM) with a JEOL JEM 2100F. Two spectrophotometers were used to measure the total spectral reflectance of the bulk samples at room temperature. Over the wavelength range from 0.25 to 2.5 μm, the near-normal (8°) hemispherical reflection spectrum was acquired using a Shimadzu UV-3600 UV-vis-NIR spectrophotometer equipped with an integrating sphere $BaSO_4$ coating of 60 mm diameter. Over the wavelength range from 2.5 μm to 16 μm, the hemispherical directional reflectance ($R \cap, \theta$) was recorded using a PerkinElmer Spectrum 100 spectrophotometer with an integrating sphere gold coating of 150 mm diameter. A mathematical treatment (Mathematica software) was used to get access to the final optical parameters such as the thermal emittance ε (in the infrared region; also referred to as spectrally averaged emissivity) and the solar absorptance α (in the UV-visible-near infrared regions; also referred to as spectrally averaged absorptivity) from the spectroscopy data, by using eqn (1) and (2), respectively:

$$\varepsilon = \frac{\int_{2.5\ \mu m}^{1.6\ \mu m}(1 - R(\lambda)) * P(\lambda)\mathrm{d}\lambda}{\int_{2.5\ \mu m}^{1.6\ \mu m}P(\lambda)\mathrm{d}\lambda} \quad (1)$$

$$\alpha = \frac{\int_{0.25\ \mu m}^{2.5\ \mu m}(1 - R(\lambda)) * G(\lambda)\mathrm{d}\lambda}{\int_{0.25\ \mu m}^{2.5\ \mu m}G(\lambda)\mathrm{d}\lambda} \quad (2)$$

With λ: the wavelength [μm], $R(\lambda)$: the spectral reflectance of the sample measured at room temperature, $G(\lambda)$: the standard solar irradiance spectrum (ASTM-G173 AM1.5 direct + circumsolar), $P(\lambda)$: the spectral emittance of a blackbody at room temperature derived from Planck's law.

Results and discussion

Synthesis and pyrolysis of Ti-modified polysilazanes

As displayed in Fig. 2a, the ATR-FTIR spectrum of PSZ shows the expected absorption bands of polysilazane; firstly, attributed to –Si–NH–Si– groups such as the N–H stretching at 3381 cm^{-1} and the vibration of the –NH unit bridging two silicon atoms at 1169 cm^{-1}.

It also highlights the typical bands of preceramic polymers containing (i) vinyl silyl groups (CH_2 = CH–Si–) *via* the bands attributed to C–H vibrations at 3058 cm^{-1}, C=C stretching at 1594 cm^{-1}, and scissoring of terminal methylene at 1404 cm^{-1}, (ii) Si-methyl groups with two bands located at 2954 and 2902 cm^{-1} and assigned to the C–H stretching and one more intense band at 1251 cm^{-1} (δ(Si–CH_3)) and (iii) Si–H groups through the strong absorption band at 2123 cm^{-1}. The largest

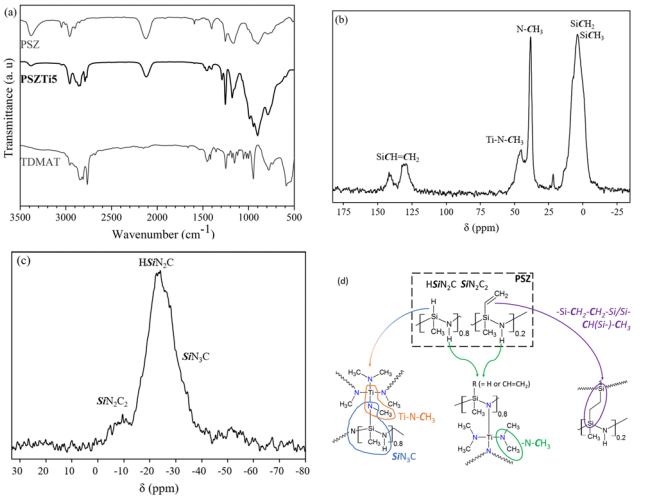

Fig. 2 (a) FTIR spectrum of PSZ, TDMAT and **PSZTi5**, (b) ^{13}C CP MAS and (c) ^{29}Si MAS NMR spectra of **PSZTi5** and (d) chemical environments identified in **PSZTi5**.

bands in the 1000–500 cm^{-1} range can be attributed to Si–N stretching in Si–N–Si units at 897 cm^{-1} and Si–C bond stretching at 787 cm^{-1} overlapping – in part – the deformation of vinyl and Si–H units.

A marked decrease in the intensity of absorption bands corresponding to N–H groups in –Si–NH–Si– units is observed in the ATR-FTIR spectrum of **PSZTi5** while new bands related to TDMAT can be detected in the wavenumber ranges of 2880–2725 cm^{-1} and 1500–1425 cm^{-1}. They can be attributed to $-N(CH_3)_x$ ($1 \leq x \leq 3$) units and more particularly to the C–H vibrations and deformation in such units, respectively. These results suggest the successful incorporation of Ti in the PSZ backbone *via* the reaction between TDMAT and NH groups in PSZ. Additionally, a decrease in the intensity of the band related to Si–H bonds is also observed, while the absorption bands at 3058 and 1594 cm^{-1} attributed to the vinyl groups strongly decreased in intensity. If considering both units, this could be explained by hydrosilylation reactions between Si–H and –Si–CH=CH_2. Although the hydrosilylation reaction usually takes place above 120 °C in pure polysilazanes,[29] previous works showed that the presence of inorganic catalysts such as transition metals or metal complexes could remarkably lower this reaction temperature.[25,30–32] However, taken separately, this can also reflect the reaction of Si–H units with TDMAT while vinyl groups polymerize.

The chemical structure of **PSZTi5** was further established by ^{13}C and ^{29}Si solid-state NMR spectroscopy (Fig. 2b and c). The cross-polarization (CP) technique has been used for ^{13}C-NMR experiments to obtain spectra with reasonable acquisition times and signal-to-noise ratios. The solid-state ^{13}C CP MAS NMR spectrum of **PSZTi5** (Fig. 2b) exhibits signals generally observed with titanium-modified polysilazane.[33] The very broad signal emerging around 3 ppm with shoulders present around 6 and 14 ppm is typical of carbon atoms of aliphatic groups bonded to a silicon atom, *i.e.*, $-SiCH_x$ ($1 \leq x \leq 3$).[34,35] The resonances at 39 and 45 ppm are assigned to $-TiNCH_3$ groups

in $N_2Si(CH_3)$–$N(CH_3)$–TiN_3 units – thus indicating the occurrence of the reaction between the silicon center of PSZ and $-N(CH_3)_2$ groups in TDMAT with the concomitant evolution of methane – and in Si_2N–TiN_3 units, respectively.[25,33] Signals at 124 and 138 ppm are attributed to the carbon of the vinyl groups present in PSZ which tend to demonstrate that hydrosilylation – suggested by FTIR – is uncomplete during the synthesis of the **PSZTi5** sample. This means that the decrease of the intensity of the Si–H band in the spectrum of **PSZTi5** is most probably ascribed to both the reaction between the silicon center of PSZ and $-N(CH_3)_2$ groups in TDMAT, hydrosilylation reaction and vinyl polymerization. The ^{29}Si MAS spectrum of the **PSZTi5** sample (Fig. 2c) is composed of a main broad resonance at around −24 ppm that can be assigned to $HSiN_2C$ environments, *i.e.*, CH_3–**Si**(H)N_2 units as present in PSZ.[34,35] In addition, there are two shoulders at around −9 ppm and −35 ppm that can be attributed to **Si**N_2C_2 and **Si**N_3C environments, respectively. These results confirm the chemical reaction between TDMAT and PSZ *via* two main mechanisms as proposed in Fig. 2d.

Our findings are in line with recently proposed mechanisms for the reaction of polycarbosilanes (Si–H) and polysilazanes (Si–H and N–H) with $-N(R)_2$ (R = CH_3 and/or CH2CH_3) ligands of the TM precursors (with TM = Ti, Zr and Hf).[36,37] The proposed reaction mechanisms also agree with our previous report on the mechanism involved in the reaction of polysilazanes with TDMAT[25,33] although, in the present paper, the hydrosilylation reaction seems to be more limited most probably because of a too low Ti content in **PSZTi5** ($[Si_{1.0}Ti_{0.2}C_{2.2}N_{1.4}H_{6.7}]_n$; oxygen content in the sample is 1.6 wt% and can be therefore neglected). Compared to the chemical formula of PSZ ($[Si_{1.0}C_{1.5}N_{1.1}H_{5.5}]_n$ (oxygen content in the sample is 0.4 wt% and can be therefore neglected), the elemental analysis data (Table 1) of **PSZTi5** confirms the successful incorporation of Ti in the backbone of PSZ in agreement with the fixed Si : Ti ratio (5) and especially the presence of $-Ti(NCH_3)_x$ (x = 1, 2) groups according to the increase of the carbon, nitrogen and hydrogen contents. The successful incorporation of $-Ti(NCH_3)_x$ (x = 1, 2) groups modifies the chemical environment around Si and N as schematically shown in Fig. 2d. It is expected to increase the crosslinking degree of PSZ (x = 1) while forming side groups which are more likely to be released in the early stage of the thermo-chemical conversion of the precursors into nanocomposites (x = 2).

Conversion of Ti-modified polysilazanes into nanocomposites

Our previous expectations are confirmed by following the weight changes of the precursors upon heat-treatment to 1800 °C by TG analysis (Fig. 3). For comparison, the TG curve of PSZ is given in the ESI† (see Fig. S1 in the ESI†). It shows that the weight changes of **PSZTi5** occur through a two-step process: (1) from room temperature (RT) to 1000 °C and (2) from 1400 to 1800 °C. Thus, in this section, we split our results and discussion into 2 parts related to each domain of temperature in which a weight loss has been identified on the TG curve (Fig. 3).

Table 1 Elemental composition of the polymers (referenced to $Si_{1.0}$)

	Element content (wt%)						
Samples	Ti	Si	C	N	O	H	Chemical formula[a]
PSZ	—	41.3	27.3	22.7	0.4	8.3	$Si_{1.0}C_{1.5}N_{1.1}H_{5.5}$
PSZTi5	10.2	30.1	29.4	21.2	1.6	7.5	$Si_{1.0}Ti_{0.2}C_{2.2}N_{1.4}H_{6.7}$

[a] Because of its low content (<2 wt%), oxygen has been omitted in the chemical formula.

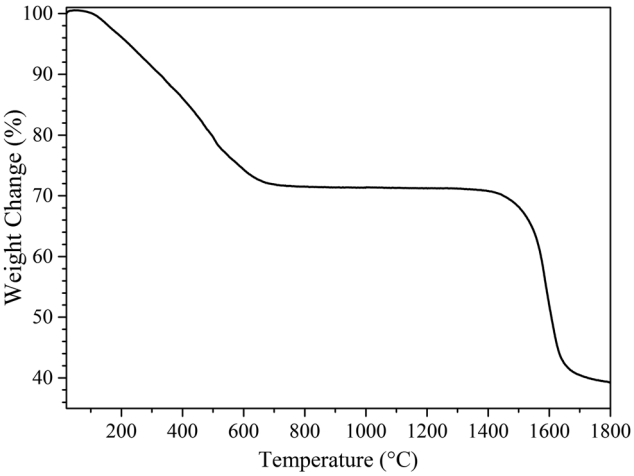

Fig. 3 TG curves of the **PSZTi5** sample recorded in flowing argon upon heat-treatment to 1800 °C.

RT to 1000 °C

In this part, we discuss the thermochemical conversion of the **PSZTi5** sample up to 1000 °C in flowing argon. **PSZTi5** showed a weight loss decreased by 5% compared to PSZ (67%) as recorded at 1000 °C.

The main difference between the two polymers occurs in the low temperature regime of the TG experiments in which volatilization of low molecular weight species takes place with PSZ. As expected, the formation of –Si–N(R)–Ti– (R = CH_3 or Si≡) units in **PSZTi5** upon chemical modification of PSZ with TDMAT tends to reduce the segment mobility of oligomeric chains; thus, limiting volatilization of small oligomeric fragments in the low temperature regime of the polymer-to-ceramic conversion. As a consequence, **PSZTi5** exhibits a reduced weight loss after decomposition at 1000 °C compared to PSZ. However, this reduced weight loss is somewhat limited most probably due to the presence of pendant groups in the form of $-Ti[(NCH_3)_2]_x$ (x = 1, 2 or 3) units that tend to be easily released as dimethylamine upon pyrolysis.

Indeed, MS (Fig. 4) demonstrated that the decomposition of **PSZTi5** is accompanied with the evolution of gaseous H_2 (m/z = 2), CH_4 and/or NH_3 (m/z = 15 and 16), ethane (m/z = 27), methylamine (m/z = 30) and dimethylamine (m/z = 44). The evolution of amine derivatives, *i.e.*, methylamine and dimethylamine, occurred earlier in the process whereas NH_3 and/or CH_4 evolutions preferentially occurred at intermediate temperatures. Amine release indicates condensation reaction between as-formed $-NCH_3-$ bridges in $N_2Si(CH_3)$–$N(CH_3)$–TiN_3 units and $-N(CH_3)_2$ groups in pendant $-Ti[(NCH_3)_2]_x$ (x = 1, 2 or 3)

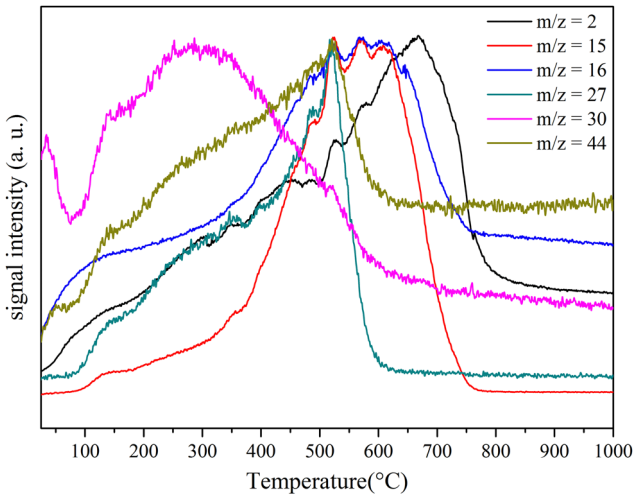

Fig. 4 MS curves recorded in the low temperature regime of the TG analysis for **PSZTi5**.

groups with residual N–H units. They represent a continuation of the reaction which occurred during the **PSZTi5** synthesis. NH_3 evolution corresponds to the transamination reaction while the CH_4 evolution originates from the decomposition of Si–CH_3. The evolution of H_2 indicates the occurrence of dehydrocoupling reactions (low temperature) as well as recombination of radicals (higher temperature) and allows forming the ceramic network labelled **PSZTi5_10** after heat-treatment at 1000 °C under argon.

The ^{29}Si MAS NMR spectrum (Fig. 5a) of the **PSZTi5_10** sample shows a large signal ranging from 0 to −50 ppm indicating a distribution of SiC_xN_{4-x} ($0 \leq x \leq 4$) units. It can nonetheless be noticed that the main peak is centered at −48 ppm corresponding to a predominant SiN_4 environment. In parallel, the X-ray diffractogram reveals that **PSZTi5_10** is poorly crystallized as shown by the diffuse peaks identified in the XRD pattern (Fig. 5b). They indicate the slow nucleation of face-centered cubic (fcc) TiC_xN_{1-x} ($0 \leq x \leq 1$) (ICDD PDF number: 00-042-1488) – which represents the complete solid solution between TiC (ICDD PDF: 00-032-1383) and TiN (ICDD PDF: 00-038-1420) – according to the presence of reflections at 2θ around 36.7° (111), 42.1° (200) and 61.5° (220). Raman spectroscopy (Fig. 5c) allows distinguishing the bands of the defect-induced D (originates from the breathing mode A_{1g} of the sp^2 rings) and graphitic G bands (arises from the stretching mode E_{2g} of the sp^2 C–C bonds) at ∼1355 cm^{-1} and ∼1590 cm^{-1}, respectively.[38]

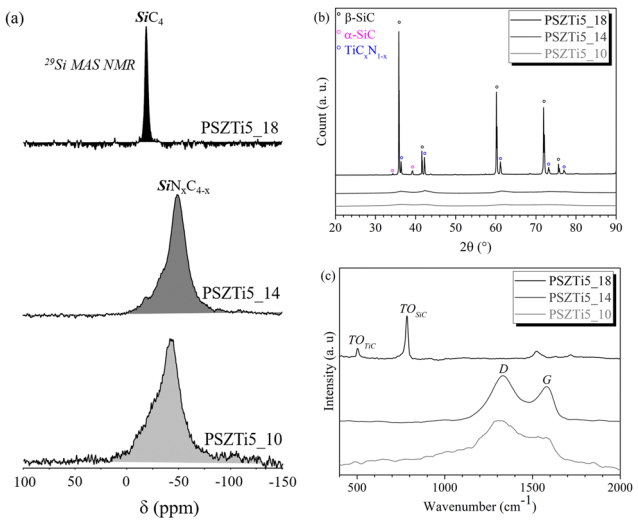

Fig. 5 (a) ^{29}Si MAS NMR spectra, (b) XRD patterns and (c) Raman spectra of **PSZTi5_*X*** samples with X = 10, 14 and 18.

The presence of free carbon is confirmed through the determination of the chemical formula ($Si_{1.0}Ti_{0.2}C_{1.3}N_{1.4}H_{0.2}$) of **PSZTi5_10** (Table 2) allowing calculating the phase content in the sample: TiN (17 wt%), Si_3N_4 (57.6 wt%), SiC (5.4 wt%) and sp^2 C (20 wt%) phases.

Analyses showed that the Si : Ti ratio fixed at the polymer level is retained in the ceramic sample prepared at 1000 °C and that the carbon and nitrogen contents increased compared to the reference PSZ_10 sample produced from PSZ under the same pyrolysis conditions. This is clearly due to the introduction of TDMAT in the PSZ network in the early stage of the process which enriches the Si environment with nitrogen and carbon.

1400 to 1800 °C

Then, we followed the high temperature behaviour of the **PSZTi5** sample by characterizing samples at 1400 °C (**PSZTi5_14**) and 1800 °C (**PSZTi5_18**) to be investigated by ^{29}Si solid-state NMR spectroscopy, X-ray diffraction and Raman spectroscopy (Fig. 5).

Solid State NMR (Fig. 5a) shows a ^{29}Si MAS NMR spectrum displaying SiN_4 units present in the **PSZTi5_14** sample (Fig. 5a). The X-ray diffractogram of the **PSZTi5_14** sample (Fig. 5b) confirmed the results obtained with the **PSZTi5_10** samples: the broad peaks at 2θ around 36.4°, 42.3°, 61.4° and 73.4° are attributed to a TiC_xN_{1-x} phase ($0 \leq x \leq 1$). Peaks related to this carbonitride phase are at the mid-position between the two references (*i.e.*, TiC and TiN) that could be approximated by Vegard's law[39] to a $TiC_{0.5}N_{0.5}$ phase. The Raman spectrum (Fig. 5c) confirms the presence of free carbon while elemental analyses show that the nitrogen content of the material is relatively stable compared to the **PSZTi5_10** sample. This confirmed that no decomposition occurred in the temperature range 1000–1400 °C as shown by TG experiments (Fig. 3).

By assessing the phase micro-/nanostructure of the **PSZTi5_14** sample by transmission electron microscopy (TEM, Fig. 6), a sample made of homogeneously dispersed small precipitates (appearing as a dark cluster in the TEM image) embedded in a featureless medium characteristic of an amorphous network is delivered. The Selected Area Electron Diffraction (SAED) pattern (insets in Fig. 6) of these small precipitates identifies poorly defined continuous rings which can be nevertheless indexed as the (111), (200) and (220) planes of the TiC_xN_{1-x} phase ($0 \leq x \leq 1$) at 0.251, 0.216 and 0.152 nm, respectively. Therefore, the material prepared at 1400 °C can be described as a nanocomposite made of TiC_xN_{1-x} nanocrystals

Table 2 Elemental composition of the samples pyrolyzed at 1000, 1400 and 1800 °C (referenced to $Si_{1.0}$)

Samples	Ti (wt%)	Si (wt%)	C (wt%)	N (wt%)	O (wt%)	H (wt%)	Chemical formula[b]
PSZ_10	—	43.6	19.1	23.2	0.2	1.1	$Si_{1.0}C_{1.0}N_{1.1}H_{0.7}$
PSZTi5_10	14.3	37.9	20.2	26.0	1.4	0.2	$Si_{1.0}Ti_{0.2}C_{1.3}N_{1.4}H_{0.2}$
PSZTi5_14	18.7[a]	40.8[a]	14.9	24.2	1.4	—	$Si_{1.0}Ti_{0.3}C_{0.9}N_{1.2}$
PSZTi5_18	15.8[a]	55.3[a]	27.4	1.3	0.2	—	$Si_{1.0}Ti_{0.2}C_{1.1}N_{0.04}$

[a] Measured by EDX. [b] Because of its low content (<2 wt%), oxygen has been omitted in the chemical formula.

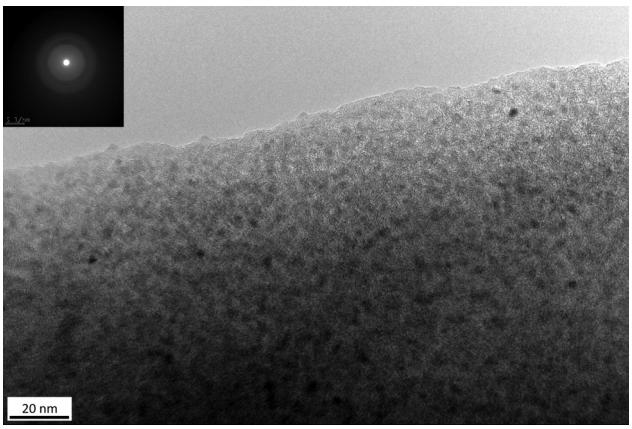

Fig. 6 High-resolution TEM image of the surface of the **PSZTi5_14** sample with the corresponding selected area electron diffraction pattern as the inset.

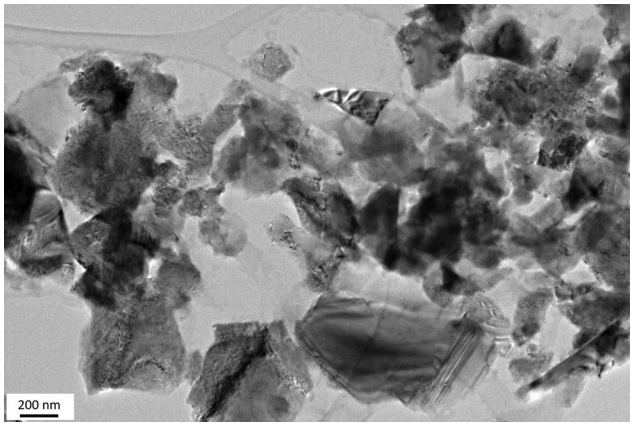

Fig. 7 TEM image representing the local structure of the **PSZTi5_18** sample.

surrounded by a poorly defined matrix; most probably made of SiC_xN_{4-x} ($0 \leq x \leq 4$) and sp^2 carbon phases as identified by solid-state NMR and Raman spectroscopy, respectively.

Above 1400 °C, Fig. 3 shows that the weight underwent a significant and continuous change up to 1700 °C. The weight loss rate then decreased in the temperature range 1700–1800 °C. Such changes are highlighted by solid-state NMR spectroscopy. The ^{29}Si MAS NMR spectrum of the **PSZTi5_18** sample completely changed (Fig. 5a): it is only composed of SiC_4 units; thus, indicating a total decomposition of SiC_xN_{4-x} ($0 \leq x \leq 4$) units identified in the **PSZTi5_10** and **PSZTi5_14** samples. This corroborates the XRD results (Fig. 5b): the XRD pattern of the **PSZTi5_18** sample identifies β- and α-SiC phases along with a TiC_xN_{1-x} ($0 \leq x \leq 1$) which can be assimilated to a $TiC_{0.7}N_{0.3}$ phase (Vegard law) based on the peak positions at 2θ = 36.4°, 42.2°, 61.1°, 73.2° and 77.0° that shifted towards TiC peak positions. The Raman spectrum of the **PSZTi5_18** sample (Fig. 5c) highlights this decomposition since it identifies the TO bands of TiC and β-SiC phases while the absence of the sp^2 carbon bands can be noticed. This indicates the complete carbothermal reduction of the Si–N bonds identified in the **PSZTi5_14** sample forming Si–C bonds in the **PSZTi5_18** sample. Carbothermal reduction reactions induce the evolution of nitrogen (See Table 2) which is responsible of the weight loss recorded by HT-TGA (Fig. 3): a weight loss of 30% has been measured in the temperature range 1400–1800 °C for the **PSZTi5_18** sample which fits relatively well the difference in terms of chemical formula between the **PSZTi5_10**/**PSZTi5_14** samples and the **PSZTi5_18** sample. Therefore, the material generated at 1800 °C can be considered as a TiC/SiC composite.

The increase of the heat-treatment temperature to 1800 °C (**PSZTi5_18** sample) fully changes the local phase micro-/nanostructure of the materials (Fig. 7). The material appears to be highly crystallized with relatively big crystals. Based on the associated EDX spectra in Fig. 8, these crystals are made of Ti and Si elements (top image) and of Si as identified in the down image. Based on EDX results, we can assume that the SAED patterns (inset in Fig. 8) identify SiC (zinc blende type, space group $F\bar{4}3m$, a = 0.436 nm) and TiC (rock-salt type, space group $Fm\bar{3}m$; a = 0.433 nm) which display close crystalline forms and lattice parameters.[40] Both SAED patterns are indeed composed of distinct spots that are ascribed to the (111), (200), (220), (311), (222), (400) and (331) planes of the cubic structures of SiC and TiC. In the following section, we investigate the effect of the structural evolution occurring from 1000 to 1800 °C on the optical properties.

Spectral selectivity of nanocomposite foams

As mentioned previously, the **PSZTi5** sample is shaped into pellets in order to investigate – as a proof of concept – the optical properties of the derived nanocomposites in the solar spectrum. Thus, we prepared the **PSZTi5_*T*** samples (T = 10, 14 and 18) by integrating a warm-pressing (WP) stage after the synthesis of **PSZTi5**. The **PSZTi5** sample exhibits sufficient plasticity to be warm-pressed at 80 °C for 30 min under 80 MPa and form crack-free pieces after pyrolysis at 1000 °C (**PSZTi5_10**). Then, the samples were heat-treated in the temperature range 1400 °C (**PSZTi5_14**) – 1800 °C (**PSZTi5_18**) in

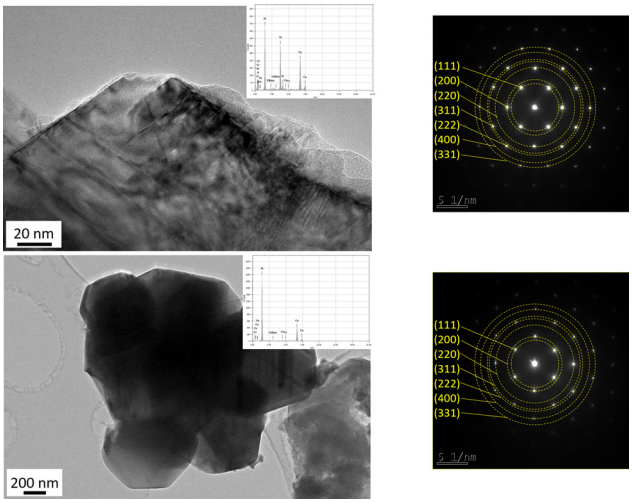

Fig. 8 TEM images of the **PSZTi5_18** sample with the corresponding EDX spectra selected area electron diffraction patterns identifying (top) TiC and (down) SiC crystals.

Table 3 Densities determined by helium pycnometry for powders (ρ_{He}) and by hydrostatic weight for bulk analogs (ρ_a apparent density, ρ_b bulk density and O.P. Open Porosity)

	Powder		Bulk analogs	
Samples	ρ_{He} (g cm^{-3})	ρ_a (g cm^{-3})	ρ_b (g cm^{-3})	O.P. (%)
PSZTi5_10	2.38	2.40	2.59	8
PSZTi5_14	2.88	2.67	2.97	10
PSZTi5_18	3.67	1.78	3.69	52

flowing argon (see Fig. S2 in the ESI†) to follow the evolution of the textural properties (Table 3) and hemispherical reflectance (Fig. 9) of pellets according to their temperature of preparation. It should be mentioned that pellets display similar XRD patterns to those recorded for powder analogs (see Fig. S3 in the ESI†).

Table 3 gathers the results obtained from the hydrostatic weight of bulk analogs (ρ_a apparent density, ρ_b bulk density and O.P. Open Porosity).

As expected, the bulk density increases with the temperature of preparation according to the extended crystallization of the materials. However, data also show that the carbothermal reduction reactions previously discussed involve a very high level of open porosity in the bulk **PSZTi5_18** samples indicating that they form foams upon heat-treatment to this temperature. The effect of the temperature of synthesis of these materials on their selectivity which is defined by the absorptance : emittance ratio[41] has been investigated. Absorptance in the solar spectrum wavelength and emittance in the infrared one are both related to hemispherical reflectance by Kirchhoff law. Fig. 9 plots the evolution of the hemispherical reflectance *versus* the wavelength for the **PSZTi_*T*** samples (T = 10, 14 and 18) at room temperature (RT). As expected, the reflectance is very low below λ = 2500 nm and is independent of the temperature of the preparation of the samples. It is close to expectation for an

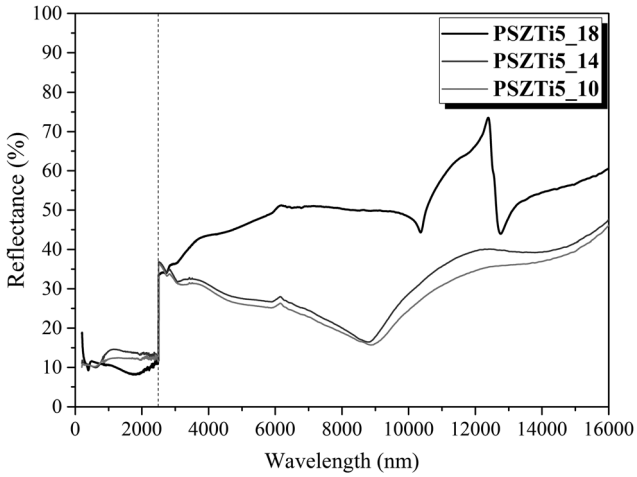

Fig. 9 Hemispherical reflectance of the **PSZTi5_X** (X = 10, 14 and 18) samples.

ideal SSA in the solar spectrum. However, the poorly crystallized samples (**PSZTi5_10** and **PSZTi5_14**) have a common non-selective behaviour with a reflectance less than 35% above 2500 nm.

The increase of the temperature of synthesis of these materials at 1800 °C provides enormous benefits. Below 2500 nm wavelength, the reflectance of the **PSZTi5_18** sample is decreased to around 10% and from 2500 to 10 000 nm, a major increase of the reflectance close to 50% is identified. At 10 000 nm, the reflectance evolves through the Christiansen point which is due to absorption mechanisms in the far-infrared range (lattice vibration), causing the material to behave like a blackbody (low reflectance = high emissivity, assuming Kirchhoff's law of radiation).[42] Thus, above 10 000 nm, the reflectance profile is characteristic of a highly crystallized SiC phase[43] in the **PSZTi5_18** sample.

The highly crystallized SiC phase in the **PSZTi5_18** sample leads to a higher hemispherical reflectance above 2500 nm and therefore a better general selectivity value (Table 4) as calculated from Fig. 9 according to eqn (1) and (2) described in the experimental part. In Table 4, we can clearly observe the contribution of the highly crystalline TiC_xN_{1-x} phase which can be assimilated to a TiC phase present in the **PSZTi5_18** sample. A RT selectivity of 1.917 has been calculated for the **PSZTi5_18** sample.

To our knowledge, this is the highest selectivity reported so far for SiC-based materials.[43–45] We should keep in mind that – in addition to the high crystal quality of the nanocomposite – one

Table 4 Optical properties calculated for the bulk samples, and an ideal solar behavior (*i.e.*, as high as possible for absorptivity and selective ratio, and as low as possible for emissivity)

Samples	α, absorptance	ε, emittance	α/ε, selectivity
PSZTi5_10	0.888	0.712	1.246
PSZTi5_14	0.882	0.684	1.289
PSZTi5_18	0.893	0.466	1.917
Ideal solar absorbers	1	0	∞

further parameter – which is not discussed here – can affect the selectivity: the porosity. Although, it is assumed that a porous structure could maximize the absorption of the solar radiation (see introduction), it has been reported that the total hemispherical emissivity can notably increase with the increase of the surface roughness/porosity.[46] For instance, an increase of the porosity from 5 to 30 vol% in HfC-based materials led to significant gain of emissivity from 0.4 to 0.55;[46] thereby a decrease of the selectivity. As a consequence, this is a property to be further investigated and we can reasonably expect an increase of the RT selectivity if dense materials (as pellets or coatings) can be prepared.

Conclusions

Within the present study, titanium-modified polysilazanes have been synthesized and used as precursors of SiC-based nanocomposites. The chemistry behind the polymer synthesis and pyrolysis was investigated in detail and the high temperature behavior of derived amorphous ceramics was critically followed. The final nano-/microstructure evolved according to the heat-treatment temperature fixed in the range of 1000–1800 °C. The amorphous single-phase ceramics produced at 1000 °C led to nanocrystalline- TiC_xN_{1-x} $(0 \leq x \leq 1)$/amorphous-SiC_xN_{4-x} $(0 \leq x \leq 4)$ nanocomposites after heat-treatment at 1400 °C. In the temperature range of 1400–1800 °C, a large weight loss occurred in the samples involving the release of nitrogen to form highly crystallized nanocomposite foams composed of TiC_xN_{1-x} $(0 \leq x \leq 1)$ and SiC crystals with free carbon. The highest optical selectivity is reached with the samples prepared at 1800 °C, which is the result of the presence of the TiC_xN_{1-x} $(0 \leq x \leq 1)$ crystals confined in the SiC matrix. The RT selectivity of these nanocomposites of 1.917 is even the highest reported for SiC-based materials despite the fact that the sample is highly porous. Thus, there is still room for further studies on optimizing the optical selectivity (not only at room temperature) of these materials by considering specific process parameters that can contribute to increase the TiC(N) volume fraction while decreasing the porosity. These opportunities are now being addressed. It can be reasonably anticipated that this will lead to SiC-based nanocomposites with a high optical selectivity.

Author contributions

MB and MC contributed equally to this work by synthesizing the materials, carrying out characterizations, analyzed and discussed the experimental data, prepared and drew the images and graphics for the publication and wrote the first draft of the manuscript. CG, AJ and XD performed selected characterization (solid-state NMR spectroscopy (CG) and optical measurements (AJ & XD)). SB (supervisor of MB and MC) supervised this research project, assisted in the material syntheses, contributed to the experimental design and data interpretation and reviewed the paper.

Conflicts of interest

There are no conflicts to declare.

Acknowledgements

Dr Samuel Bernard, Dr Maxime Balestrat, and Dr Xavier Deschanels acknowledge Agence Nationale de la Recherche (ANR) for supporting this work through the Carapass project (PhD thesis of Maxime Balestrat, Project No. ANR-16-CE08-0026-01). Dr Samuel Bernard thanks the Nouvelle-Aquitaine region and CTTC for the financial support of the PhD thesis of Maxime Cheype.

Notes and references

1 Q. Chen, Y. Wang, J. Zhang and Z. Wang, *Energies*, 2020, **13**, 1988.
2 F. Cao, K. McEnaney, G. Chen and Z. Ren, A review of cermet-based spectrally selective solar absorbers, *Energy Environ. Sci.*, 2014, **7**, 1615–1627.
3 L. Noč and I. Jerman, *Sol. Energy Mater. Sol. Cells*, 2022, **238**, 111625.
4 J. Mandal, D. Wang, A. C. Overvig, N. N. Shi, D. Paley, A. Zangiabadi, Q. Cheng, K. Barmak, N. Yu and Y. Yang, *Adv. Mater.*, 2017, **29**, 1702156.
5 C. E. Kennedy, *Review of Mid- to High-Temperature Solar Selective Absorber Materials*, National Renewable Energy Lab., Golden, CO. (US), 2002.
6 J. J. Cuomo, J. F. Ziegler and J. M. Woodall, *Appl. Phys. Lett.*, 1975, **26**, 557–559.
7 I. Cañadas, V. M. Candelario, G. De Aloysio, J. Fernández, L. Laghi, S. Cuesta-López, Y. Chen, T. J. Marrow, A. Rinaldi, A. M. Sanchez, A. Tatì and C. Testani, *Materials*, 2021, **14**, 4627.
8 M. J. H. Balat, *J. Eur. Ceram. Soc.*, 1996, **16**, 55–62.
9 C. Verdon, O. Szwedek, A. Allemand, S. Jacques, Y. Le Petitcorps and P. David, *J. Eur. Ceram. Soc.*, 2014, **34**, 879–887.
10 E. Sani, L. Mercatelli, F. Francini, J.-L. Sans and D. Sciti, *Scr. Mater.*, 2011, **65**, 775–778.
11 E. Sani, L. Mercatelli, P. Sansoni, L. Silvestroni and D. Sciti, *J. Renewable Sustainable Energy*, 2012, **4**, 033104.
12 E. Sani, L. Mercatelli, J.-L. Sans, L. Silvestroni and D. Sciti, *Opt. Mater.*, 2013, **36**, 163–168.
13 V. Ern and A. C. Switendick, *Phys. Rev.*, 1965, **137**, A1927–A1936.
14 E. Sani, L. Mercatelli, M. Meucci, A. Balbo, L. Silvestroni and D. Sciti, *Sol. Energy*, 2016, **131**, 199–207.
15 K. Xu, M. Du, L. Hao, J. Mi, Q. Yu and S. Li, *J. Materiomics*, 2020, **6**, 167–182.
16 H. Aréna, M. Coulibaly, A. Soum-Glaude, A. Jonchère, A. Mesbah, G. Arrachart, N. Pradeilles, M. Vandenhende, A. Maitre and X. Deschanels, *Sol. Energy Mater. Sol. Cells*, 2019, **191**, 199–208.

17 H. Aréna, M. Coulibaly, A. Soum-Glaude, A. Jonchère, G. Arrachart, A. Mesbah, N. Pradeilles, M. Vandenhende, A. Maître and X. Deschanels, *Sol. Energy Mater. Sol. Cells*, 2020, **213**, 110536.
18 B. Du, X. Wang and Z. Zou, *Tribol. Lett.*, 2011, **43**, 295–301.
19 P. J. Martin, R. P. Netterfield, W. G. Sainty and C. G. Pacey, *J. Vac. Sci. Technol., A*, 1984, **2**, 341–345.
20 S. Shimada and T. Ishil, *J. Am. Ceram. Soc.*, 1990, **73**, 2804–2808.
21 S. Shimada, *Solid State Ionics*, 2002, **149**, 319–326.
22 A. Onuma, H. Kiyono, S. Shimada and M. Desmaison, *Solid State Ionics*, 2004, **172**, 417–419.
23 M. C. Bechelany, A. Lale, M. Balestrat, C. Gervais, S. Malo, R. K. Nishihora and S. Bernard, *J. Eur. Ceram. Soc.*, 2022, **42**, 4172–4178.
24 M. C. Bechelany, V. Proust, A. Lale, M. Balestrat, A. Brioude, C. Gervais, R. K. Nishihora and S. Bernard, *J. Eur. Ceram. Soc.*, 2022, **42**, 2135–2145.
25 M. Balestrat, A. Lale, A. V. A. Bezerra, V. Proust, E. W. Awin, R. A. F. Machado, P. Carles, R. Kumar, C. Gervais and S. Bernard, *Molecules*, 2020, **25**, 5236–5258.
26 M.-C. Bechelany, V. Proust, C. Gervais, R. Ghisleny, S. Bernard and P. Miele, *Adv. Mater.*, 2014, **26**, 6548.
27 A. Lale, A. Wasan, R. Kumar, P. Miele, U. B. Demirci and S. Bernard, *Int. J. Hydrogen Energy*, 2016, **41**, 15477–15488.
28 M. Wynn, D. Lopez-Ferber, A. Viard, D. Fonblanc, M. Schmidt, F. Rossignol, P. Carles, G. Chollon, C. Gervais and S. Bernard, *Open Ceram.*, 2021, **5**, 100055.
29 N. S. Choong Kwet Yive, R. J. P. Corriu, D. Leclercq, P. H. Mutin and A. Vioux, *Chem. Mater.*, 1992, **4**, 141–146.
30 J. Wang, V. Schölch, O. Görke, G. Schuck, X. Wang, G. Shao, S. Schorr, M. F. Bekheet and A. Gurlo, *Open Ceram.*, 2020, **1**, 100001.
31 S. Tada, M. D. Mallmann, H. Takagi, J. Iihama, N. Asakuma, T. Asaka, Y. Daiko, S. Honda, R. K. Nishihora, R. A. F. Machado, S. Bernard and Y. Iwamoto, *Chem. Commun.*, 2021, **57**, 2057–2060.
32 N. Asakuma, S. Tada, E. Kawaguchi, M. Terashima, S. Honda, R. K. Nishihora, P. Carles, S. Bernard and Y. Iwamoto, *Nanomaterials*, 2022, **12**, 1644–1659.
33 M. C. Bechelany, V. Proust, A. Lale, P. Miele, S. Malo, C. Gervais and S. Bernard, *Chem. – Eur. J.*, 2017, **23**, 832–845.
34 D. Fonblanc, D. Lopez-Ferber, M. Wynn, A. Lale, A. Soleilhavoup, A. Leriche, Y. Iwamoto, F. Rossignol, C. Gervais and S. Bernard, *Dalton Trans.*, 2018, **47**, 14580–14593.
35 A. Viard, D. Fonblanc, M. Schmidt, A. Lale, C. Salameh, A. Soleilhavoup, M. Wynn, P. Champagne, S. Cerneaux, F. Babonneau, G. Chollon, F. Rossignol, C. Gervais and S. Bernard, *Chem. – Eur. J.*, 2017, **23**, 9076–9090.
36 Q. Wen, Y. Xu, B. Xu, C. Fasel, O. Guillon, G. Buntkowsky, Z. Yu, R. Riedel and E. Ionescu, *Nanoscale*, 2014, **6**, 13678–13689.
37 J. Yuan, S. Hapis, H. Breitzke, Y. Xu, C. Fasel, H.-J. Kleebe, G. Buntkowsky, R. Riedel and E. Ionescu, *Inorg. Chem.*, 2014, **53**, 10443–10455.
38 M. Balestrat, E. Diz Acosta, O. Hanzel, N. Tessier-Doyen, R. Machado, P. Šajgalík, Z. Lenčéš and S. Bernard, *J. Eur. Ceram. Soc.*, 2020, **40**, 2604–2612.
39 P. Duwez and F. Odell, *J. Electrochem. Soc.*, 1950, **97**, 299–304.
40 N. R. Mediukh, V. I. Ivashchenko, P. E. A. Turchi, V. I. Shevchenko, J. Leszczynski and L. Gorb, *Calphad*, 2019, **66**, 101643.
41 J. D. Macias, D. M. Herrera-Zamora, F. I. Lizama-Tzec, J. Bante-Guerra, O. E. Arés-Muzio, G. Oskam, H. R.-P. Rubio, J. J. Alvarado-Gil, C. Arancibia-Bulnes, V. Ramos-Sánchez and H. I. Villafán-Vidales, *AIP Conf. Proc.*, 2017, **1850**, 120001.
42 B. Rousseau, J. F. Brun, D. D. S. Meneses and P. Echegut, *Int. J. Thermophys.*, 2005, **26**, 1277–1286.
43 M. Coulibaly, G. Arrachart, A. Mesbah and X. Deschanels, *Sol. Energy Mater. Sol. Cells*, 2015, **143**, 473–479.
44 E. Sani, L. Mercatelli, D. Jafrancesco, J. L. Sans and D. Sciti, *J. Eur. Opt. Soc. Rap. Public.*, 2012, **7**, 12052.
45 X. Xu, Z. Rao, J. Wu, Y. Li, Y. Zhang and X. Lao, *Sol. Energy Mater. Sol. Cells*, 2014, **130**, 257–263.
46 E. Sani, L. Mercatelli, J.-L. Sans, L. Silvestroni and D. Sciti, *Opt. Mater.*, 2013, **36**, 163–168.